Research Square

Preprints are preliminary reports that have not undergone peer review.
They should not be considered conclusive, used to inform clinical practice,
or referenced by the media as validated information.

Lake-catchment system responses to mercury and lead pollution from industrial activities in Mediterranean environments: legacy controls and current recovery dynamics in Lake Estanya (NE Spain)

Isabel Rodríguez-Veiga
Centro de Investigaciones Energéticas, Medioambientales y Tecnológicas
Jorge Pey
Instituto Pirenaico de Ecología
Antonio Garralón
Centro de Investigaciones Energéticas, Medioambientales y Tecnológicas
Virginia Peyres
Centro de Investigaciones Energéticas, Medioambientales y Tecnológicas
Thomas Schmid
Centro de Investigaciones Energéticas, Medioambientales y Tecnológicas
Mario Morellón
Universidad Complutense de Madrid
Blas L. Valero-Garcés
Instituto Pirenaico de Ecología
Marcel Saïd Galofre Penacho
Instituto Andaluz de Ciencias de la Tierra
Bastien Duval
CEA Cadarache
David Amouroux
Institut des Sciences Analytiques et de Physico-Chimie pour l'Environnement et les Matériaux
Rocio Millán
Centro de Investigaciones Energéticas, Medioambientales y Tecnológicas
Juan Pablo Corella
pablo.corella@mncn.csic.es

Museo Nacional de Ciencias Naturales

Research Article

Keywords: Mercury, lead, lake sediments, chlor-alkali industry, legacy pollution, atmospheric deposition

Posted Date: August 12th, 2026

DOI: https://doi.org/10.21203/rs.3.rs-10575554/v1

License: This work is licensed under a Creative Commons Attribution 4.0 International License.
Read Full License

Additional Declarations: No competing interests reported.

Abstract

Mercury (Hg) and lead (Pb) are persistent, toxic trace metals whose pollution legacy from industrial activities can remain in the environment for centuries until reaching long-term sinks. This study reconstructs the history of Hg and Pb accumulation in Lake Estanya (NE Spain), a karstic lake system located 30 km downwind of the industrial complex of Monzón, known for hosting chlor-alkali, metallurgical and chemical industries. Two gravity cores retrieved in 2023 were analysed at sub-decadal resolution, spanning the last 330 years of evolution in Hg and Pb concentrations, enrichment factors, accumulation fluxes, and Pb isotopic composition. Analysis of atmospheric deposition samples from Monzón further enabled characterisation of the pollution processes currently affecting the Estanya catchment, allowing a comparison between legacy contamination and present-day trends.

The sedimentary record reveals a rise in Hg and Pb accumulation during the second half of the twentieth century, synchronous with the establishment and expansion of the chemical industry in Monzón, the intensification of metallurgical activity, and the widespread use of leaded gasoline together with growing road traffic in Spain prior to its ban in 2001. Hg and Pb enrichment factors and accumulation fluxes increased exponentially from 1950 onward, followed by a marked decline at the turn of the 21st century, attributed to the effectiveness of environmental regulations and the resulting reduction in primary Hg and Pb emissions. This trend is supported by the Pb isotopic signature, which shifts toward more radiogenic values in recent decades, indicating incipient system recovery. Nonetheless, Pb and especially Hg concentrations and enrichment factors remain elevated, reflecting the persistence of these trace metals and the formation of reservoirs that sustain their recycling decades after primary emissions ceased. Source apportionment of recent atmospheric deposition attributes Hg and Pb inputs to a mixture of industrial emissions, road traffic, and dust from regional sources and Saharan outbreaks.

These results show that, while emission inputs are rapidly reflected in lake sediment records, system recovery is delayed by the long-term persistence and remobilisation of legacy Hg and Pb. This finding highlights the relevance of high-resolution lake records for tracking industrial pollution trajectories, enabling assessment of the effectiveness of environmental regulations and ecosystem recovery.

Introduction

Mercury (Hg) and lead (Pb) are among the most environmentally significant trace metal pollutants due to their toxicity, persistence, and capacity for long-range atmospheric transport. These trace elements are natural constituents of the Earth's crust, and their distribution was primarily controlled by geogenic processes (Cullen and McAlister 2017; Streets et al. 2017). However, increasing anthropogenic forcing has profoundly altered their global biogeochemical cycles, resulting in significant rise in atmospheric emissions and environmental accumulation in aquatic and terrestrial ecosystems (Driscoll et al. 2013; Horowitz et al. 2014; Cullen and McAlister 2017; Streets et al. 2017).

Human activities such as ore mining, fossil fuel combustion, metal processing, chemical manufacturing and biomass burning have contributed to the widespread dispersal of Hg and Pb. Once emitted into the atmosphere, these trace metals may remain airborne over variable periods, enabling transboundary transport before being deposited onto soils, vegetation and inland waters. There, they can persist for decades to centuries depending on environmental conditions and biogeochemical cycling (Horowitz et al. 2014; Semertzidou et al. 2016; Streets et al. 2017). This long-term accumulation has contributed to soil degradation and the persistent contamination of aquatic ecosystems, particularly in industrialised regions (Driscoll et al. 2013; Cheng et al. 2025). Therefore, given their ubiquitous distribution, recalcitrance, toxicity and bioaccumulative potential, Hg and Pb have been classified as pollutants of special concern, needing careful environmental monitoring (Hylander and Meili 2003; Cullen and McAlister 2017; Eklöf et al. 2024). Although major environmental regulations and technological improvements implemented during the late twentieth century have substantially reduced trace metal emissions, the response of natural systems is often delayed due to the persistence of contaminants stored in catchment soils and sediments (Bacardit et al. 2012; Driscoll et al. 2013). Consequently, evaluating not only the onset and magnitude of contamination, but also the timing and trajectory of environmental recovery, is essential for understanding the long-term legacy of industrial pollution and the resilience of lake ecosystems to anthropogenic stress (Corella et al. 2017; Eklöf et al. 2024; Hooler et al. 2025).

Natural archives provide unique opportunities to reconstruct pollution histories and evaluate environmental responses over decadal to centennial timescales. Among these, lake sediments are particularly valuable because they integrate atmospheric deposition, catchment-derived inputs and internal lake processes, preserving continuous records of contaminant accumulation over time (Mills et al. 2017; Cooke et al. 2020; Sabatier et al. 2022). Sedimentary sequences enable assessment of catchment responses to cumulative contaminant burdens, revealing whether reductions in emissions are reflected in sedimentary archives and quantifying environmental recovery in response to pollution control policies (Gascón Díez et al. 2017; Elbaz-Poulichet et al. 2020; Rosca et al. 2024). In the Iberian Peninsula, paleolimnological studies have successfully reconstructed the long-term dynamics of atmospheric metal pollution in mountain lakes and remote high-altitude environments (Bacardit et al. 2012; Corella et al. 2017; Hillman et al. 2017; Corella et al. 2018; 2021; Rodriguez-Iruretagoiena et al. 2023; Duval et al. 2025; Morellón et al. 2025). However, relatively few studies have addressed lakes located near major industrial centres (Rodriguez-Veiga et al. 2026), where sedimentary archives can directly record local atmospheric contamination superimposed on broader regional signals and provide valuable insights into the pace of environmental recovery following emission reductions.

Within this context, *Balsas de Estanya* offers an exceptional setting for investigating the long-term impact of industrial emissions in the southern Pyrenean foreland. This karstic lake system, located in northeastern Spain, has been widely studied for its continuous Holocene sedimentary record and high sensitivity to environmental change, making it one of the best-characterised lacustrine archives in the Iberian Peninsula (Morellón et al. 2008; López-Vicente et al. 2009; Morellón et al. 2009a; 2009b; Valero-Garcés et al. 2009; Morellón et al. 2011; Navas et al. 2013; Gaspar et al. 2020). Its proximity to Monzón—

one of the main industrial centres of northeastern Spain during the twentieth century—makes it particularly suitable for evaluating the atmospheric legacy of industrial emissions. Monzón hosts major metallurgical and chemical industries, including a chlor-alkali plant historically recognised as a potential source of atmospheric Hg emissions, together with Pb-bearing industrial activities (Raldúa et al. 2007; Gascón Roche 2019; Pey et al. 2020; Ayuntamiento de Monzón 2022). The lake lies downwind of the industrial area under prevailing regional wind conditions, enhancing its sensitivity to atmospheric transport of industrial aerosols and gases. This makes it an ideal natural archive for investigating both pollution histories and subsequent recovery trajectories. Preliminary studies of the lake provided information related to the trace metals enrichments (Corella et al. 2018) and mercury biogeochemical cycling (Duval et al. 2025). However, the poor chronological resolution of the studied sedimentary sequences has limited the evaluation of metal loading during the industrial period.

In this study, we present a high-resolution reconstruction of Hg and Pb accumulation over the last ~ 330 years based on a newly dated sedimentary sequence from Lake Estanya. This decadal resolution archive is complemented by modern atmospheric deposition measurements in the Monzón area, allowing direct comparison between historical sediment accumulation and present-day atmospheric inputs (Pey et al. 2026). The integration of Pb isotopic signatures, enrichment factors, and recent depositional data allows for a high-resolution reconstruction of industrial contamination phases while distinguishing natural backgrounds from anthropogenic inputs. Particular attention is given to the long-term trajectories of Hg and Pb, whose current elevated levels underscore the challenges posed by their environmental accumulation and the subsequent formation of reservoirs that act as secondary emission sources long after industrial activities have ceased (Driscoll et al. 2013; Cullen and McAlister 2017). Beyond its regional significance, this study provides new insights into the response times of lake-catchment systems to industrial contamination and the persistence of pollution legacies in Mediterranean environments.

Study site

Lake Estanya (officially *Balsas de Estanya*; 42°02' N, 0°32' E; 670 m a.s.l.) is a low altitude karstic lake complex located in the Southern Central Pyrenees, near the northern boundary of the Ebro River Basin (Fig. 1a). Geologically, this system is situated within a small basin (2.45 km^2) that forms part of a more extensive Miocene polje. The bedrock consists of low-permeability Upper Triassic marls and claystones (Keuper facies), whereas Middle Triassic limestones and dolostones (Muschelkalk facies) dominate the higher elevations of the catchment (Sancho Marcén 1988). Upper Triassic carbonate and evaporite outcrops favoured intense karstification, leading to the development of several dolines and depressions, some of which are infilled with Quaternary sediments (Sancho Marcén 1988; Morellón et al. 2011). The system comprises three main dolines containing permanent water (Fig. 1b). The largest and deepest, *Estanque Grande de Abajo* (hereafter referred to as Lake Estanya), consists of two sub-basins separated by a ridge above the water surface (Morellón et al. 2011). The southern sinkhole, with a maximum water

depth of 20 m, has been the subject of several paleolimnological studies (Morellón et al. 2008; 2009a; 2009b; 2011) and is the primary focus of the present study.

Hydrogeologically, Lake Estanya is an endorheic system due to the low permeability of the basin bedrock and the absence of permanent surface drainage. Consequently, the hydrological balance is dominated by groundwater inputs from the local aquifer, whereas evaporation is the principal water loss. Several ephemeral streams contribute to sporadic inflow during runoff events (López-Vicente et al. 2009; Morellón et al. 2009a; 2009b; 2011).

Lake Estanya is a brackish, oligotrophic, and monomictic system characterised by sulphate and calcium-rich water (Morellón et al. 2009a; 2009b; 2011). Thermal stratification of the lake water occurs during spring and summer months, leading to anoxic hypolimnetic conditions, which facilitates the preservation of organic matter. Algal productivity and alkalinity also peak during the summer (Ávila et al. 1984; Morellón et al. 2009a). During winter, the water column is fully mixed, and displays uniform temperature and oxygen levels throughout (Morellón et al. 2009a). Lake level fluctuations during the last decades have been mostly controlled by the occurrence of pluriannual drought periods.

There is strong evidence of significant human impact in Estanya during the last 2000 years, characterised by alternating periods of intensive and extensive land use (Riera et al. 2004; Morellón et al. 2009b). In the last 40 years, mechanisation of agricultural activities has led to higher nutrient input to the lake system (Morellón et al. 2011). Since 1997, Estanya has been protected under regional legislation and is currently integrated into the European Natura 2000 Network as a Site of Community Importance (SCI) (Navas et al. 2013).

The lake is located in a Mediterranean-continental climate zone with intense summer drought and extreme rainfall events during spring and autumn. The annual accumulated precipitation reaches 471 mm, exceeded by the estimated evapotranspiration of 774 mm (Morellón et al. 2011). The mean annual temperature is 14.3°C, ranging from 4.7°C in January to 24.6°C in July, with maxima regularly exceeding 37°C (AEMET).

Lake Estanya is close to the heavily industrialised town of Monzón, located 30 km southwest of the lake. In the 1950s, this area underwent a rapid transition from an agrarian economy to a major industrial centre due to its strategic logistical location, excellent connectivity to key industrial nodes and the lack of emission regulations at the time. The local industry focused on two primary sectors: heavy chemical synthesis—notably the synthesis of chlorine derivatives, polyvinyl chloride, calcium carbide—and metallurgy, comprising silicomanganese and ferromanganese furnaces for ferroalloy production (Gascón Roche 2019; Ayuntamiento de Monzón 2022). Industrial development and diversification continued throughout the second half of the 20th century, turning the area into a major pollution hotspot (Raldúa et al. 2007; Corral-Broto and Ortega Santos 2021). Currently, modern industries have successfully adopted cleaner standards and stricter regulation policies; however, the environmental legacy of past operations remains a persistent issue today.

An atmospheric deposition monitoring station operates in Monzón (41.92°N, 0.19°E; 279 m a.s.l.). Classified as an industrial background site within the DONAIRE network, the station is influenced by local industrial emissions, regional and road dust resuspension, and coal-fuel burning (Pey et al. 2020), besides of natural contributions from North African dust outbreaks (Pey et al. 2026). During the 2016–2017 monitoring campaign, bulk atmospheric deposition fluxes accounted for 29.2 g m^{-2} yr^{-1}, with insoluble and soluble fractions contributing nearly equally to the total mass deposition (14.7 and 14.5 g m^{-2} yr^{-1}, respectively) (Pey et al. 2020). Given its proximity to Lake Estanya, this station provides crucial reference data for assessing atmospheric inputs to the watershed and evaluating their imprint on the geochemical composition of sedimentary records.

Material and methods

Fieldwork and sediment sampling

Two short gravity cores of 41 cm and 46 cm long (LEG23-1A-1G and LEG23-1B-1G respectively) were retrieved in March 2023 from the deepest part of the main lake within the Estanya karstic lake system using a UWITEC gravity corer (Fig. 1c). Core LEG23-1A-1G was subsampled at 0.5 cm intervals and the samples were freeze-dried for subsequent geochemical analyses. Dry bulk density was estimated from the wet and dry sample weights. Core LEG23-1B-1G was split lengthwise and imaged at high-resolution with a Multi-Sensor Core Logger (MSCL) at the Pyrenean Institute of Ecology (IPE-CSIC, Saragossa, Spain).

Geochemical analyses

Total Hg content was quantified via atomic absorption spectroscopy using a Direct Mercury Analyser (DMA-80 evo, Milestone srl, Italy) in accordance with EPA 7473 Method (U.S. EPA 1998). Instrument accuracy was verified using a certified reference material (NCS DC87103, soil, [Hg] = 0.017 ± 0.003 mg kg^{-1}) showing a detection limit of 0.003 ng. The analytical precision was consistent, with an RSD < 10% (mean RSD = 4.7%; n = 82). Results were reported in mg kg^{-1} of dry weight sediment.

Pb concentration was determined by mass spectrometry using high-resolution inductively coupled plasma mass spectrometry (Element II SF-ICP-MS; Thermo Finnigan, Bremen, Germany). Sample digestion was conducted in a microwave oven “BERGHOF MWS” in closed Teflon vessels with 2 M HNO_3 (15 ml). After digestion, dried precipitate was diluted with 2% (v/v) high-purity HNO_3 and filtered at 0.45 µm following EPA 3050B method (U.S. EPA 1996). Elemental concentration is expressed in mg kg^{-1} of dry weight sediment. Aluminium (Al) and zinc (Zn) content in discrete sediment samples were analysed by X-ray fluorescence (XRF) using the Counter Top XRF analyser (CTX; Bruker, U.S.), operating at 30 kV, 20 mA, and a counting time of 90 s. The results were expressed as mg kg^{-1}. Total Carbon (TC) and Total Inorganic Carbon (TIC) were determined by combustion of dried samples in a Total Organic Carbon analyser (SSM 5000A; Shimadzu, Japan). For TIC analysis, sample pre-treatment with 28% phosphoric

acid (H_3PO_4) was required. Total Organic Carbon (TOC) was calculated as the difference between TC and TIC.

Hg and Pb mass accumulation rates were calculated based on each element concentration in the sediment (mg kg^{-1}), the dry bulk density (g cm^{-3}) and the sedimentation rates (cm yr^{-1}) obtained from the age-depth model in accordance with Givelet et al. (2003). Mass accumulation rates were expressed in µg m^{-2} yr^{-1}. Enrichment Factors (EFs) for Hg and Pb were estimated using Al normalisation to decouple pollution signals from variations in lithogenic inputs. Al was chosen as reference element due to its geochemical stability and high abundance in carbonate-rich catchments. EFs were calculated by comparison with the baseline conditions, defined as the average concentration of the last 5 cm.

$$EF = \frac{\raisebox{1ex}{\$}\left[M_{cm}\right]\$\Big/\raisebox{-1ex}{\$}\left[Al_{cm}\right]\$}{\raisebox{1ex}{\$}\left[M_{bottom}\right]\$\Big/\raisebox{-1ex}{\$}\left[Al_{bottom}\right]\$}$$

1

$[M_{cm}]$ and $[Al_{cm}]$ refer to metal (Hg or Pb) and Al concentrations at equivalent depths, while $[M_{bottom}]$ and $[Al_{bottom}]$ correspond to the metal (Hg or Pb) and Al concentrations in the basal layers of the Lake Estanya sequence. However, it is worth noting that basal conditions must not be considered as natural background conditions since anthropogenic activities have influenced the area since the Middle Ages (Riera et al. 2004; 2006; Valero-Garcés et al. 2009; Morellón et al. 2011; González-Sampériz et al. 2017).

Sediment core correlation and age-depth model

The chronology for core LEG23-1A was established through stratigraphic correlation with previously dated Estanya core 1A-1M (Morellón et al. 2011) (ESM_1, Fig. S1). TOC (%) content was used as the primary geochemical proxy to correlate both records. To validate the correlation, ^{137}Cs activity was measured in core LEG23-1A via gamma spectrometry using a coaxial-type Extended-Range HPGe detector (Canberra) at 0.5 cm resolution. The ^{137}Cs peaks identified in the LEG23-1A profile were compared with the reference ^{137}Cs profile from core 1A-1M to ensure correlation consistency.

Lead isotope analyses

To identify the potential sources of Pb contamination in the Estanya sediment core, a high-resolution Pb isotope analysis was performed at 0.5 cm intervals. Samples of 0.1 g from each of the 82 samples were digested overnight in high-purity HNO_3 (65%, analytical reagent grade; Scharlab, Barcelona, Spain) and evaporated to dryness. The residue was then dissolved in 0.5 M ammonium acetate for Pb separation from major cations by conventional ion exchange chromatography (DigiSEP Blue, SCP Science). Recovered Pb was evaporated to dryness, dissolved in high-purity 0.5 M HNO_3 and diluted to a final concentration of 100–200 ppb. Quantification of ^{204}Pb, ^{206}Pb, ^{207}Pb, and ^{208}Pb was determined by sector-field inductively coupled plasma mass spectrometry using an Element II SF-ICP-MS (Thermo Finnigan, Bremen, Germany) operating at low-resolution mode ($m/\Delta m \approx 300$). Analytical reliability was ensured by

employing the standard bracketing method during sample measurement. All chemical solutions were prepared with high-purity deionised water (18.2 MΩ·cm). For calibration, NIST 981 reference material was diluted using 2% high-purity HNO_3. Further details regarding the method, reagents and materials used can be found in Rodriguez-Veiga et al. (2026).

Atmospheric deposition fluxes

During an annual high-resolution campaign, bulk deposition was collected every ~ 15 days in the industrial site of Monzón to quantify temporal variations in atmospheric deposition of major and trace elements. All samples were processed to determine both soluble and insoluble fractions following the procedures described in Pey et al. (2020) for soluble deposition, and Pey et al. (2026) for insoluble species. In the soluble fraction, major anions were measured by ion chromatography (881 Compact IC Pro, Metrohm), whereas cations and HCO_3^- were analysed using a continuous flow analyser (Alliance Futura, Alliance Instruments). In addition, dissolved trace metals (Ag, Al, As, Ba, Cd, Co, Cr, Cu, Fe, Mn, Mo, Ni, Pb, Sb, Se, Th, Tl, V, Zn) were quantified after acidification of 50 ml aliquots with 5% HNO_3 by ICP-MS (Varian Vista MPX). The insoluble fraction was determined gravimetrically using the 47 mm quartz fibre filters employed in the filtration of each collected sample. After gravimetry, ¾ of each filter was used for geochemical analyses to determine elemental concentrations (Ag, Al, As, Ba, Be, Ca, Cd, Cl, Co, Cr, Cu, Fe, K, Mg, Mn, Mo, Na, Ni, Pb, Sb, Se, Sr, Th, Ti, Tl, U, V, Zn) using inductively coupled plasma, atomic emission spectroscopy and mass spectrometry (ICP-AES and ICP-MS, respectively) after acid digestion of filters in a HNO_3:HF:$HClO_4$ mixture of Suprapur-grade HNO_3, HF and $HClO_4$ acids (Merck, Darmstadt, Germany), as described in Pey et al. (2026). In addition, total Hg content was analysed in filter samples (thus, only the insoluble fraction) by atomic absorption spectrophotometry (AMA 254, LECO Company), with no specific preservation treatment to reduce Hg loss during sampling. Due to the low availability of remaining sample after prior determinations, Hg concentrations were recovered in 13 out of 27 samples through matrix correlation with Fe, Mn, and Sr, with results reported as range values. Positive Matrix Factorization (PMF 5.0, U.S. EPA (2014)) was used to identify and quantify potential sources contributing to the measured variables. Uncertainties were calculated according to the method proposed by Amato et al. (2009) (see ESM_1, Appendix A and ESM_2 for further details).

Results

Age model

The age-depth model for core LEG23-1A was developed after linear interpolation between the established tie-points with core 1A-1M using the R package “clam” (Blaauw 2010) (ESM_1, Fig. S2). The 1963 atmospheric nuclear testing maximum, identified at 14–15 cm, and a secondary peak identified at 8–9 cm, potentially attributed to the 1986 Chernobyl accident in core 1A-1M (Morellón et al. 2011), correlate with the ^{137}Cs peaks observed at 16 cm and 7 cm in the new LEG23-1A sequence. The coherence between ^{137}Cs activity profiles for core LEG23-1A and 1A-1M ensure the robustness of the age model. The base of the sequence corresponds to ca. 1700 CE, spanning the last ~ 330 years.

Geochemistry and sedimentology

Three lithostratigraphic units, previously described by Morellón et al. (2011), were identified based on visual and compositional analysis in core LEG23-1A (Fig. 2). Unit 3 (41–35 cm; 1690–1760 AD) comprises bedded organic silts (average TOC: 1.7%) organised in cm-thick layers with intercalations of gypsum and aragonite laminae. Concentrations of Hg and Pb display their lowest values in the record (basal level: 0.03 and 7.57 mg kg^{-1}, respectively) and increase progressively up-core. Unit 2 (35–15 cm; 1760–1965 AD) features variegated laminae consisting of alternating clays, organic-rich laminae, and silts. Reduced detrital influx from the watershed is coupled with increased organic (average TOC: 3.3%) and inorganic (average TIC: 2.7%) productivity. Mean Hg concentration double relative to basal values (Unit 2 mean Hg content = 0.11 mg kg^{-1}) and Pb content maintains an increasing trend (averaging 12.82 mg kg^{-1}). Unit 1 (15–0 cm; 1965–present) displays alternating dark grey and black organic-rich silts in cm-thick layers. In this unit, TIC and TOC reach their maximum values (5.9 and 5.1%, respectively) reflecting highest organic and carbonate productivity of the whole sequence. Mean Hg shows a six-fold increase over basal values, with a maximum peak reaching 0.5 mg kg^{-1}. Mean Pb content in unit 1 doubles its basal concentration (unit 1 mean Pb content = 14.85 mg kg^{-1}). Sedimentation rates (SR) exhibit a gradual increase, varying between 0.81 and 1.16 mm yr^{-1} in units 3 and 2, and peaking at 3.19 mm yr^{-1} in unit 1. The increase in SR reflects enhanced contributions from both authigenic (gypsum and carbonate) and detrital fluxes within the watershed.

Enrichment factors and lead isotope signatures

Lake Estanya sediments exhibit an overall upward enrichment trend in Hg and Pb throughout the core (Fig. 3). Two distinct stages were identified in the enrichment profiles.

The first stage (pre-1950) exhibits minimum EF values for Hg and Pb (Hg = 0.77, Pb = 0.91) and is characterised by a moderate and relatively stable increase, with mean values of 2.2 and 1.4, respectively. During this interval, the lead isotopic profile shows an antithetic trend, showing radiogenic values at the core base ($^{206}Pb/^{207}Pb$ = 1.204) that gradually decrease to 1.192 by the end of the period. Similarly, Hg/Zn and Pb/Zn ratios show a steady, gradual increase.

The second stage (post-1950) is marked by an abrupt rise in trace metals enrichment. The mean Hg EF reaches 8.5 during this period, representing a four-fold increase over basal levels. Since the 1980s, Hg EFs increase exponentially, reaching peak values of 21.3 in the uppermost centimetres of the record. Pb enrichment also displays a sharp increase during the 1960s that persists up-core (Pb EF mean = 2.5) with intermittent peaks of up to 3.7. Concurrently, $^{206}Pb/^{207}Pb$ profile underwent an abrupt decrease from 1.192 in the 1950s to 1.178 in the 1990s, synchronous with the exponential increase in Hg EFs. By the early 21st century, $^{206}Pb/^{207}Pb$ ratios had returned to more radiogenic values, reaching 1.187 in the uppermost centimetre of the core. Likewise, the Hg/Zn and Pb/Zn ratios show a significant increase, closely mirroring the Hg and Pb EF profiles respectively.

Hg and Pb accumulation fluxes in Lake Estanya sediments

The sedimentary record from Lake Estanya enabled a sub-decadal reconstruction of Hg and Pb depositional fluxes over the last ~ 330 years (Fig. 4). Hg and Pb accumulation fluxes show a coupled, increasing trend across two well-defined phases (Fig. 4a). Prior to 1950, Hg accumulation rates remained low displaying minimal variability, ranging between 20 and 52 μg m^{-2} yr^{-1} with a mean value of 33 μg m^{-2} yr^{-1}. Conversely, the Pb flux displayed a more oscillating profile during this period, with values ranging from 2076 to 9590 μg m^{-2} yr^{-1}.

The accumulation rate profiles changed in the post-1950 era showing a drastic, synchronous surge in both Hg and Pb fluxes. This sawtooth pattern contrasts sharply with the relatively stable pre-1950 interval. The mean Hg accumulation rate rose to 158 μg m^{-2} yr^{-1}, representing nearly a five-fold increase over baseline levels. Three peaks can be distinguished: 146 (ca. 1961 CE), 229 (ca. 1994 CE), and a record 402 μg m^{-2} yr^{-1} at the turn of the century (ca. 2001 CE). Pb fluxes also experienced a pronounced increase, with a mean value of 10524 μg m^{-2} yr^{-1} for the last 70 years (two times the Pb basal values). The Pb profile also shows three well-defined peaks: 20873 (ca. 1961 CE), 15498 (ca. 1986 CE) and a peak of 21956 μg m^{-2} yr^{-1} (ca. 1998 CE). Both Hg and Pb fluxes underwent a sharp, concurrent decline in the early 2000s, averaging 83 and 2343 μg m^{-2} yr^{-1} respectively. This downward trend has persisted to the present, with contemporary accumulation rates reverting to pre-1950 values (Hg = 52 μg m^{-2} yr^{-1}, Pb = 1223 μg m^{-2} yr^{-1}, ca. 2023 CE).

Accumulation fluxes in atmospheric deposition filters

The annual high-resolution monitoring campaign, conducted at the Monzón industrial site, enabled the reconstruction of atmospheric Hg and Pb deposition fluxes (Fig. 4b). Between June 2016 and June 2017, the mean annual Hg insoluble flux was 10 μg m^{-2} yr^{-1}, with values ranging from late March (2 μg m^{-2} yr^{-1}) to a maximum in late January (23 μg m^{-2} yr^{-1}). For the same period, the mean Pb insoluble flux was 961 μg m^{-2} yr^{-1}; notably, the Pb lowest value (178 μg m^{-2} yr^{-1}) coincided with the Hg minimum in late March, while its maximum occurred in February (2564 μg m^{-2} yr^{-1}). Although a marginal trend toward higher deposition was observed during autumn and winter months, no significant correlation was found between precipitation and trace metal deposition fluxes (Hg $r = 0.10$, $p = 0.64$; Pb $r = 0.36$, $p = 0.09$).

Source apportionment analysis

Source apportionment analysis of the atmospheric insoluble samples identified seven PMF factors that explain the deposition patterns of Hg and Pb in the region (Fig. 5). The seven PMF factors were interpreted according to their dominant elemental and chemical signatures: 1) Local and regional dust, traced by Ca and Sr, and enhanced amounts of P, explains around 20% of atmospherically deposited Hg and less than 10% of deposited Pb. 2) Road traffic is characterised by organic and elemental carbon (OC and EC) and trace elements associated to brake and tyre wear -such as Sb, Ba, Zn and Cu (Amato et al.

2009); overall, accounting for ~ 20% of atmospherically deposited Hg and 30% of deposited Pb. 3) Regional pollution + aged sea spray were traced by secondary inorganic aerosols (nitrate and sulphate) and most of Na^+ and Cl^- concentrations, with very low amounts of other aerosol species; overall explaining less than 10% of atmospherically deposited Hg and Pb. 4) Industrial emissions are traced by Mn, Co and Ca, and explain up to 20 and 25% of atmospherically deposited Hg and Pb, respectively. 5 and 6) Two factors were associated with combustion of mixed sources, which together represent ~ 10% of deposited Hg and Pb. These factors are characterised by high OC and EC contents, together with elevated concentrations of trace elements such as Se, Sn, Pb, and Sb as well as a very strong contribution of Ca^{2+} and HCO_3^-, likely associated with industrial processes. 7) African dust, enriched in mineral elements including Al, Fe, Ti, K, Na, and V, consistent with that reported from African dust sources by Bandrés et al. (2026) and Pey et al. (2026), explaining around 20% of atmospherically deposited Hg and Pb.

Discussion

Historical evolution of Hg and Pb contamination: trace metal enrichment and Pb isotopes fingerprint

The combined analysis of Hg and Pb concentrations, enrichment factors, elemental ratios and Pb isotopic composition provides a comprehensive framework for reconstructing the history of trace metal contamination recorded in the Lake Estanya sediments. As the geochemical records display distinct temporal patterns before and after the mid-twentieth century, these two periods are discussed separately to clarify the processes and pollution sources controlling the observed trends.

To identify the factors controlling trace-metal accumulation before and after the onset of industrialisation, correlation patterns between trace metals and Al, Zn, TOC and TIC were evaluated separately for the pre- and post-1950 periods (ESM_1- Table S1). Before 1950, Hg and Pb were negatively correlated with Al ($r = -0.61$ and $r = -0.36$, respectively), indicating that their variability was not primarily controlled by changes in detrital input. Instead, the positive correlation between Hg and Pb ($r = 0.72$), together with their strong relationship with Zn (Hg–Zn: $r = 0.63$; Pb–Zn: $r = 0.70$), suggests a common source, most likely associated with coal burning, regional mining and metallurgical activities as seen in other Pyrenean records (Corella et al. 2021). Likewise, the strong correlation of both metals with TOC (Hg–TOC: $r = 0.86$; Pb–TOC: $r = 0.66$) could suggest that organic matter played an important role in the scavenging and burial of trace metals under pre-industrial conditions.

From the late seventeenth century to the mid-nineteenth century, Hg and Pb concentrations remained relatively low, showing only modest increases throughout the record. This pattern is consistent with enrichment factors close to baseline values (Hg EF = 1.4; Pb EF = 1.1), suggesting limited anthropogenic influence beyond natural geochemical variability and diffuse regional mining and smelting emissions (Corella et al. 2017). During this period, human activities within the Lake Estanya catchment were largely restricted to agricultural land use (Riera et al. 2004; Morellón et al. 2011; González-Sampériz et al. 2017), supporting the interpretation that most trace metal inputs originated from regional atmospheric

deposition and the progressive runoff of accumulated heavy metals on soils in previous decades rather than local sources. This interpretation is further supported by the Pb isotopic composition, which exhibits the most radiogenic values of the entire sequence (mean $^{206}Pb/^{207}Pb$ = 1.204). These values are consistent with data from other pre-industrial sediment records (Millot et al. 2004; Kylander et al. 2010; Adánez Sanjuán et al. 2018) (Fig. 6).

Between approximately 1850 and 1950, Hg and Pb concentrations increased more noticeably, accompanied by a moderate rise in enrichment factors. Pb EF increased to ≈ 1.8, whereas Hg EF reached values close to 3.3, indicating that Hg responded more strongly than Pb during the early stages of industrialisation. In parallel, $^{206}Pb/^{207}Pb$ ratio progressively decreased to 1.192, reflecting the increasing contribution of anthropogenic Pb (Adánez Sanjuán et al. 2018). Similar Hg and Pb enrichments have been reported from other lake sediment records in the Pyrenees and NE Iberian Peninsula (Corella et al. 2017; 2018; 2021), suggesting that this pattern reflects the regional atmospheric imprint of nineteenth- and early twentieth-century industrialisation rather than local contamination.

Following the mid-twentieth century, the geochemical trends observed in the previous period changed significantly. This transition is evidenced by the decoupling of Hg, Pb and Zn, with Hg becoming the dominant pollutant during this period. Likewise, Hg and Pb lost their strong association with TOC, indicating that trace-metal accumulation was no longer primarily controlled by organic matter scavenging but by increasingly important external inputs.

Hg exhibits the most pronounced response to post-1950 industrialisation. Hg enrichment factors increased abruptly after the 1950s (EF Hg ≈ 4.5) and accelerated exponentially from the late 1980s onwards, reaching maximum EF values exceeding 21 in the uppermost sediment layers. The magnitude of Hg enrichment largely exceeds that reported from other Pyrenean records (Corella et al. 2017; 2018; 2021; Rodriguez-Iruretagoiena et al. 2023), where Hg accumulation mainly reflects the regional atmospheric signal associated with increased industrial emissions driven by the diversification of Hg uses across Southwestern Europe (Horowitz et al. 2014; Streets et al. 2017). Consequently, the exceptional Hg enrichment recorded in Lake Estanya cannot be explained solely by the magnification of industrial emissions and coal burning for energy production, but instead, indicates the impact of nearby industrial sources that dominated Hg accumulation throughout the second half of the 20th century. A comparable departure from the regional atmospheric signal has previously been documented in Lake Chiprana (NE Spain), where Hg and Pb enrichment factors also increased markedly after the mid-twentieth century in response to local industrial emissions associated with coal combustion, reaching maximum values of 7.8 and 23, respectively (Rodriguez-Veiga et al. 2026).

Historical industrial activities in Monzón since the 1950s have been directly linked to trace metal emissions, primarily Hg and Pb. Key contributing industrial processes include synthesis of chlorine and by-products via mercury cell electrolysis, metal smelting, alloy synthesis or cement manufacturing (Horowitz et al. 2014; Cullen and McAlister 2017; Cheng et al. 2025; Javanmardi and Berton 2025). The abrupt increase in Hg EFs during the 1990s is synchronous with documented production peaks in the

local chlor-alkali industry (OSPAR Commission 2019). Concurrently, Pb pollution exhibited a steady increase, likely driven by the widespread use of anti-knocking additives in gasoline, which was punctuated by maximum spikes linked to output increases in the regional metallurgical sector.

Such Hg and Pb EF excursions are in good agreement with a synchronous decline in the $^{206}Pb/^{207}Pb$ isotopic signature, which reached minimum values in the mid-90s ($^{206}Pb/^{207}Pb = 1.179$) (Fig. 6). This shift reflects a complex change in the mixture of local pollution sources, resulting in less radiogenic Pb isotopic compositions due to the sustained use of lead derived from diverse ores with lower $^{206}Pb/^{207}Pb$ signatures (Adánez Sanjuán et al. 2018). Also, Duval et al. (2025) analysed Hg isotopic signatures in Lake Estanya sediments, documenting a positive shift in the δ202Hg and Δ199Hg during the industrial period, probably linked to the intensification of industrial activities in Monzón industrial complex. The onset of the 21st century brought the implementation of stricter environmental regulations, including the 2001 ban on leaded gasoline in Spain (RD 785/2001 2001) and the transition to membrane technology in chlor-alkali plants (OSPAR Commission 2019). The impact of these measures is evidenced by a recovery of the Pb isotopic values ($^{206}Pb/^{207}Pb = 1.187$) observed in the upper sediment layers.

Despite the efforts in the implementation of cleaner production methods, Hg and Pb enrichment factors have remained high in recent years. This effect may be attributed to the inherent persistence of trace metals in the environment and their susceptibility to remobilisation, allowing for the recycling of Hg and Pb between different ecological compartments until they eventually reach long-term sinks after several decades to centuries. Thus, regional contaminated soils act as a surface reservoir enabling trace metal re-emission, posing a significant issue for current environmental recovery (Bacardit et al. 2012; Driscoll et al. 2013; Streets et al. 2017; Eklöf et al. 2024).

Past and present trends in trace metal accumulation fluxes: Hg and Pb legacy pollution and recovery

Hg and Pb accumulation in Lake Estanya sediments over the last 330 years

Both Hg and Pb accumulation fluxes display similar long-term evolution, with relatively low values before 1950 contrasting with a marked increase during the second half of the 20th century. Accumulation rates peaked between the 1980s and early 2000s, followed by a rapid decline over the last two decades. Unlike enrichment factors, however, accumulation fluxes are influenced not only by changes in trace-metal loading but also by variations in sedimentation rates. The lower SR after the 1940s is consistent with the progressive depopulation of the region and the abandonment of intensive agricultural practices (Valero-Garcés et al. 2009; Morellón et al. 2011). Conversely, the increase in SR observed during recent decades has been attributed to mechanisation of the farming activities and the remobilisation of littoral sediments, rather than general enhanced catchment erosion (Morellón et al. 2011). Therefore, the temporal evolution of Hg and Pb accumulation fluxes reflects the combined influence of fluctuating atmospheric trace-metal inputs and sediment accumulation processes. Nonetheless, the abrupt post-

1950 increase in Hg and Pb fluxes cannot be explained by sedimentation rate changes alone, indicating a substantial increase in atmospheric trace-metal deposition during this period.

Post-1950 Hg fluxes in Lake Estanya (158 μg m^{-2} yr^{-1}) contrast sharply with those reported from other lakes in the region during this period, such as Lake Marboré (~ 40 μg m^{-2} yr^{-1}), where peaks coincided with the maximum production at Almadén between 1960 and 1970 (Hylander and Meili 2003; Corella et al. 2021). In contrast, our results are more consistent with accumulation fluxes from other low-altitude lakes impacted by local industrial activity, like Lake Chiprana, where modern research shows a mean Hg flux of 260 μg·m^{-2}·yr^{-1}, peaking up to 2000 μg·m^{-2}·yr^{-1} in 1957 (Rodriguez-Veiga et al. 2026). Although the global downward trend in Hg emissions began after the 1970s (Horowitz et al. 2014; Streets et al. 2017), the decline in Hg accumulation rates in Lake Estanya is not observed until the turn of the 21st century. We attribute this abrupt yet delayed decline to the combination of three key factors: (1) the implementation of stringent Hg-emission controls and the subsequent switch to membrane technology within the Monzón chlor-alkali plant (ca. 2011–2015) (OSPAR Commission 2019), (2) the global reduction in industrial Hg use due to increased awareness about its toxicity, and (3) the closure of the Almadén mine in 2003 (Hylander and Meili 2003; Horowitz et al. 2014; Corella et al. 2021).

In the last two decades and despite the implementation of industrial Hg-emission controls, Hg concentrations in the uppermost sediment layers remain well above pre-industrial levels and consistently exceed the Threshold Effect Level (TEL = 0.174 mg kg^{-1}; MacDonald et al. (2000)). The presence of Hg at the sediment-water interface is of particular concern, as it is highly susceptible to exhibit significant concentrations in pore waters leading to benthic remobilisation and transfer to the water column (Guédron et al. 2020). There, Hg can undergo physicochemical transformations which modify its bioavailability, such as bacterial methylation under anaerobic conditions, facilitating its entry into the food web (Duval et al. 2023). Furthermore, Hg deposited in soils and surface waters is susceptible to photochemical reduction to gaseous Hg^0, leading to its re-emission into the atmosphere and subsequent redistribution across and within ecosystems. In semi-arid regions, this process is enhanced by greater solar irradiance, drought periods, and increased wind turbulence (Driscoll et al. 2013). This indicates that legacy Hg contamination remains a significant environmental concern despite the reduction in primary emissions, because re-emission from impacted surfaces continues to redistribute Hg across surface reservoirs and thus maintaining high Hg fluxes even after emission sources have ceased (Driscoll et al. 2013; Pey et al. 2020; Eklöf et al. 2024).

Although post-1950 Pb accumulation fluxes display a temporal evolution broadly similar to that of Hg, their trajectories diverge during recent decades. The increase in Pb accumulation rate in Lake Estanya during this period is consistent with other Pyrenean records (Corella et al. 2017; 2018; 2021; Rodriguez-Veiga et al. 2026) reflecting the exponential rise in atmospheric Pb deposition driven by the widespread use of leaded gasoline and the rapid growth of road traffic after 1950 (Schwikowski et al. 2004). However, Lake Estanya exhibits much higher accumulation rates compared to other mid-elevation lakes in the region, such as Montcortès (which peaked between 1953 and 1971 with mean Pb AR 5920 μg·m^{-2}·yr^{-1}; (Corella et al. 2017)). This discrepancy suggests that Pb deposition in Lake Estanya reflects

the combined contribution of multiple local industrial sources, which may have contributed to the regional Pb burden. Industrial activities in Monzón directly associated to Pb emissions—such as metal smelting, cement manufacturing and alloy production—along with fluctuations in their production output, likely account for the sawtooth profile observed in the Pb accumulation rate. Unlike the 1970s European trend, which saw a widespread decline in Pb emissions due to gasoline additive regulations and improved de-dusting installations, the decrease in Lake Estanya Pb fluxes was delayed until the onset of the 21st century, coinciding with the ban and progressive phase-out of leaded gasoline in Spain (RD 785/2001 2001; Pacyna et al. 2007).

Contemporary trends in Hg and Pb accumulation and source apportionment analysis

In order to elucidate current Hg and Pb depositional dynamics, accumulation fluxes were measured in atmospheric deposition samples during the 2016–2017 period. The results obtained were compared with Hg and Pb sedimentary fluxes obtained for the same interval to determine the connectivity between both records.

Despite exhibiting similar deposition trends, neither Hg nor Pb showed a single source origin nor a well-defined deposition pattern. Hg deposition flux showed no correlation with the amount of precipitation ($r = 0.1$, $p = 0.64$). While the literature typically reports a positive correlation between Hg deposition and rainfall, the underlying deposition mechanism is modulated by factors such as chemical speciation, regional precipitation regimes, proximity to industrial emission sources, and particle size distribution of emissions. Some studies (Sakata et al. 2006; 2008) identified a positive correlation between wet Hg flux and precipitation in humid regions, however, dry deposition of trace metals predominates in industrialised areas (Amodio et al. 2014). This dominance is likely driven by the emission of coarse particles and short-lived Hg species, which create local deposition hotspots (Driscoll et al. 2013). Landis et al. (2004) showed that reactive gaseous mercury (RGM) from mercury-cell chlor-alkali plants has a higher dry deposition velocity than elemental or particulate Hg. Furthermore, in arid regions where rainfall is scarce and suspended dust loads are high—such as the Ebro Depression—dry deposition prevails over wet deposition (Enrico et al. 2016). Consequently, wind-driven re-emission of Hg, combined with allochthonous aerosol contributions acting as Hg carriers (e.g., Saharan dust), may account for current deposition fluxes, despite the 2015 decommissioning of mercury-cell technology at the Monzón plant (Driscoll et al. 2013; Pey et al. 2020).

Pb deposition fluxes were likewise non-significantly related to precipitation ($r = 0.4$, $p = 0.09$), consistent with dry-deposition-dominated regimes documented in industrialized settings. Sakata et al. (2006) and Amodio et al. (2014) found markedly elevated dry deposition fluxes of Pb at industrial and urban sites relative to background sites, attributing this enhancement to coarse metallurgical particles with short atmospheric residence times that are largely decoupled from precipitation scavenging. In Monzón, approximately 55% of the insoluble deposition flux originated from currently operational local industrial

sources. Notably, these include silicomanganese and ferromanganese furnaces, a calcium carbide plant, and cement manufacturing plant, all of which emit large quantities of particulate matter that likely govern the insoluble Pb deposition flux at present (Pey et al. 2026).

Our results suggest that atmospheric Hg and Pb deposition does not follow clear seasonal patterns; instead, deposition is driven by site-specific factors, including local climatology and strong industrial influence. Nonetheless, the limited sample size (n = 27) constrains the statistical robustness of these observed patterns. Future long-term studies will be useful to corroborate the presence or absence of deposition patterns linked to seasonality. Furthermore, as the soluble fraction for Hg was not determined and gaseous Hg losses were not taken into account, current Hg deposition fluxes are, probably, considerably underestimated. For Pb, the soluble contribution along the year was 124 μg m^{-2} and the insoluble 988 μg m^{-2}. Therefore, 85% of Pb deposition was recorded in the insoluble fraction, despite its mobilisation to the soluble fraction can occur thereafter.

Finally, to identify the primary recent emission sources of Hg and Pb, a source attribution analysis was performed on the atmospheric deposition samples (Fig. 5). Source apportionment analysis further demonstrates that present-day atmospheric Hg deposition results from the combined influence of both natural and anthropogenic sources. Hg deposition is distributed almost equally among regional and local dust, African dust intrusions, road traffic and industrial emissions, each accounting for approximately 20% of the total Hg deposition. The importance of regional dust highlights the role of Hg remobilisation from previously contaminated soils and sediments within the semi-arid Ebro Valley, one of the main dust-emitting regions of the Iberian Peninsula (Pey et al. 2020). Likewise, long-range transport of Saharan dust provides an additional pathway for atmospheric Hg deposition through the adsorption of oxidised Hg species onto mineral particles (Souza et al. 2025). Anthropogenic contributions are primarily associated with industrial emissions and road traffic, including both exhaust and non-exhaust emissions, as well as the resuspension of Hg-enriched road dust.

Lead exhibits a broadly similar source signature, although road traffic represents the dominant contributor (29.6%), followed by industrial emissions (22.4%) and African dust (20.6%). Together, these results indicate that contemporary atmospheric Hg and Pb deposition reflects the integrated contribution of multiple natural and anthropogenic sources rather than a single dominant emitter. This interpretation is consistent with the sedimentary record, where Hg and Pb display distinct temporal trends while both record the cumulative influence of industrial development and regional atmospheric transport over the last three centuries.

Comparison of recent sedimentary and atmospheric deposition records

Contemporary trace-metal deposition trends were assessed by comparing data from atmospheric deposition filters at the Monzón monitoring station and accumulation fluxes in recent sediment layers. Despite representing different environmental compartments, Hg and Pb fluxes are of the same order of

magnitude in both archives. Specifically, Hg accumulation rates were 10 vs 97 μg m^{-2} yr^{-1}, while Pb accumulation rates reached 961 vs 2282 μg m^{-2} yr^{-1} in the atmospheric filters and sediments, respectively. These results indicate that recent Hg and Pb accumulation in Lake Estanya sediments provides a realistic estimate of contemporary atmospheric trace-metal deposition, reinforcing the interpretation that lake sediments constitute reliable environmental archives capable of recording long-term changes in atmospheric trace-metal loading. A similar scenario has been previously reported in Lake Chiprana (Rodriguez-Veiga et al. 2026). During the 2016–2017 campaign, insoluble atmospheric fluxes reached 3.2 μg m^{-2} yr^{-1} for Hg and 709 μg m^{-2} yr^{-1} for Pb, while recent sedimentary fluxes exhibited values of 28 μg m^{-2} yr^{-1} for Hg and 895 μg m^{-2} yr^{-1} for Pb. The Hg accumulation rates reported for both atmospheric deposition and sediments in Lake Estanya are at least three times higher than those recorded in Lake Chiprana. This discrepancy is reasonable and is likely attributable to the legacy contamination associated with the Monzón chlor-alkali industry and the spread and accumulation of this contamination in all compartments of Lake Estanya watershed. Pb accumulation rates in Lake Estanya likewise exceed those recorded in Lake Chiprana, however, whereas the increase in atmospheric filters is modestly higher (by a factor of 1.3), sedimentary fluxes are four times higher, a difference that may be explained by the multiple Pb-emitting sources in Monzón, which remain active to this day.

The combined sedimentary and atmospheric records highlight the different timescales over which anthropogenic forcing and lake-system recovery operate. The rapid decline in Hg accumulation fluxes following the implementation of emission-control measures indicates that reductions in atmospheric emissions are rapidly transferred to the sedimentary record. In contrast, the persistence of elevated Hg concentrations in the uppermost sediments, demonstrates that the environmental legacy of past contamination persists long after atmospheric inputs have declined. This decoupling between the rapid reduction in external forcing and the slower recovery of sediment quality emphasises that the response of lake systems to anthropogenic perturbations is not instantaneous, but reflects the long-term impact of accumulated contaminants. This phenomenon is especially relevant in certain regions, such as the Ebro Valley, in which regional dust remobilisation is common, generating a continuous atmospheric pool of legacy pollution. In this context, the Lake Estanya sequence demonstrates that high-resolution paleolimnological records provide a unique opportunity to quantify both the immediate response and the long-term recovery trajectory of lake systems subjected to intense anthropogenic perturbations.

Conclusions

This study provides a high-resolution, ~ 330-year reconstruction of Hg and Pb accumulation in Lake Estanya, complemented by trace metal atmospheric deposition measurements at the nearby Monzón industrial complex, allowing a direct comparison between the legacy sedimentary record and present-day pollution inputs. The combined use of trace metal concentrations, enrichment factors, accumulation fluxes and Pb isotopic signatures enabled the identification of two contamination phases: a pre-1950 period dominated by natural geochemical processes and diffuse regional inputs, followed by a moderate increase linked to regional industrialisation, and an abrupt post-1950 rise, driven by the expansion of local industrial emissions related to chlor-alkali and metallurgical industry. The subsequent decline in Hg

and Pb fluxes and the shift toward more radiogenic Pb isotopic compositions since the late twentieth century suggest early environmental recovery, driven by the effectiveness of environmental regulations, including the 2001-ban on leaded gasoline and the conversion of the Monzón chlor-alkali plant to membrane technology. However, sediment enrichment and source apportionment data indicate that dust resuspension, Saharan intrusions, industry, and traffic persist as Hg and Pb sources, showing that legacy contamination in the catchment continues to act as a secondary emission source. The close agreement between recent sedimentary fluxes and atmospheric deposition rates further confirms that Lake Estanya sediments faithfully record contemporary trace-metal loading, validating this archive as a reliable tool for tracking both historical contamination and ongoing recovery. Overall, these results show that while reductions in primary emissions are rapidly transmitted to the sedimentary record, the recovery of the ecosystem is often delayed due to the persistence and remobilisation of legacy Hg and Pb, underscoring the long-term environmental risk posed by industrial pollution legacies in Mediterranean settings and highlighting the value of high-resolution paleolimnological archives for evaluating the pace and trajectory of ecosystem recovery.

Declarations

Author Contribution

I.R-V. and J.P.C. conceived and designed the study. J.P. led the atmospheric deposition monitoring and analysis in Monzón. V.P. supervised the gamma spectrometry measurements for ^{137}Cs dating. I.R-V., J.P.C., M-S.G.P., T.S., performed fieldwork and sediment sampling. I.R-V. carried out the geochemical analyses. A.G. performed the elemental composition and Pb isotope analyses. M.M. and B.V.G. contributed the chronological framework and stratigraphic correlation. D.A. and B.D. contributed to the interpretation of mercury biogeochemical data. R.M. contributed to the discussion and interpretation of the results. I.R-V., J.P.C., wrote the original draft. All authors reviewed and approved the final manuscript.

Acknowledgement

Financial support has been received from the national project POSAHPI (PID2022-143146OB-I00, Spanish National Research Plan) and by the MONIMER project (CPP2024-011432; MICIU/AEI, and FEDER-EU, Public–Private Collaboration Projects programme). A CIEMAT predoctoral grant (213-PRECIE-PDM22) provided additional financial support. Further funding was received through the PALEONET network (RED24-153734-T), financed by the Spanish Ministerio de Ciencia, Innovación y Universidades, the Agencia Estatal de Investigación, and FEDER (EU). The authors would like to extend their gratitude to Nuria Navarro and Marcos Mejuto from the Ionizing Radiation Metrology Laboratory (CIEMAT) for their support and assistance during the gamma spectrometry analysis.

References

1. Adánez Sanjuán P, Flem B, Llamas Borrajo JF, García Cortés Á, Locutura Rupérez J (2018) Lead isotopic composition of overbank sediments in areas with different anthropogenic and lithological characteristics. Water Air Soil Pollut 229:172. https://doi.org/10.1007/s11270-018-3831-0
2. AEMET (Agencia Estatal de Meteorología). Climatologías mensuales/anuales Benabarre (2022):https://opendata.aemet.es/centrodedescargas/ (Accessed: 12/03/2026).
3. Amato F, Pandolfi M, Escrig A, Querol X, Alastuey A, Pey J et al Hopke PK (2009) Quantifying road dust resuspension in urban environment by multilinear engine: a comparison with PMF2. Atmos Environ 43:2770–2780. https://doi.org/10.1016/j.atmosenv.2009.02.039
4. Amodio M, Catino S, Dambruoso PR, de Gennaro G, Di Gilio A, Giungato P et al Tutino M (2014) Atmospheric deposition: sampling procedures, analytical methods, and main recent findings from the scientific literature. Adv Meteorol 2014:161730. https://doi.org/10.1155/2014/161730
5. Ávila A, Burrel JL, Domingo A, Fernández E, Godall J, Llopart JM (1984) Limnología del Lago Grande de Estanya (Huesca). Oecol Aquat 7:3–24.
6. Ayuntamiento de Monzón (2022) Economía. Ayuntamiento de Monzón. https://www.xn--monzn-3ta.es/econom%C3%ADa. Accessed 14 May 2026
7. Bacardit M, Krachler M, Camarero L (2012) Whole-catchment inventories of trace metals in soils and sediments in mountain lake catchments in the Central Pyrenees: apportioning the anthropogenic and natural contributions. Geochim Cosmochim Acta 82:52–67. https://doi.org/10.1016/j.gca.2010.10.030
8. Bandrés J, López-Moreno JI, Salvador P, Pey J (2026) Chemistry and sources of atmospheric aerosols deposited in the Central Pyrenees in the period 2016–2023, with a focus on African dust events occurred during cold season. Atmos Res 331:108686. https://doi.org/10.1016/j.atmosres.2025.108686
9. Blaauw M (2010) Methods and code for 'classical' age-modelling of radiocarbon sequences. Quat Geochronol 5:512–518. https://doi.org/10.1016/j.quageo.2010.01.002
10. Cooke CA, Martínez-Cortizas A, Bindler R, Sexauer Gustin M (2020) Environmental archives of atmospheric Hg deposition – a review. Sci Total Environ 709:134800. https://doi.org/10.1016/j.scitotenv.2019.134800
11. Corella JP, Saiz-Lopez A, Sierra MJ, Mata MP, Millán R, Morellón M et al Valero-Garcés BL (2018) Trace metal enrichment during the Industrial Period recorded across an altitudinal transect in the Southern Central Pyrenees. Sci Total Environ 645:761–772. https://doi.org/10.1016/j.scitotenv.2018.07.160
12. Corella JP, Sierra MJ, Garralón A, Millán R, Rodríguez-Alonso J, Mata MP et al Valero-Garcés BL (2021) Recent and historical pollution legacy in high altitude Lake Marboré (Central Pyrenees): a record of mining and smelting since pre-Roman times in the Iberian Peninsula. Sci Total Environ 751:141557. https://doi.org/10.1016/j.scitotenv.2020.141557
13. Corella JP, Valero-Garcés BL, Wang F, Martínez-Cortizas A, Cuevas CA, Saiz-Lopez A (2017) 700 years reconstruction of mercury and lead atmospheric deposition in the Pyrenees (NE Spain).

Atmos Environ 155:97–107. https://doi.org/10.1016/j.atmosenv.2017.02.018

14. Corral-Broto P, Ortega Santos A (2021) A simple overflow?: environmental coloniality in francoist Spain (1950–1979). Perspect J Polit Sci 25:29–42. https://doi.org/10.21814/perspectivas.3564
15. Cullen JT, McAlister J (2017) Biogeochemistry of lead. Its release to the environment and chemical speciation. In: Metal ions in life sciences. https://doi.org/10.1515/9783110434330-002
16. Cheng X, Wang S, Chen J, AghaKouchak A (2025) Global assessment and hotspots of lake drought. Commun Earth Environ 6:308. https://doi.org/10.1038/s43247-025-02285-2
17. Díaz-Somoano M, Suárez-Ruiz I, Alonso JIG, Ruiz Encinar J, López-Antón MA, Martínez-Tarazona MR (2007) Lead isotope ratios in Spanish coals of different characteristics and origin. Int J Coal Geol 71:28–36. https://doi.org/10.1016/j.coal.2006.05.006
18. Driscoll CT, Mason RP, Chan HM, Jacob DJ, Pirrone N (2013) Mercury as a global pollutant: sources, pathways, and effects. Environ Sci Technol 47:4967–4983. https://doi.org/10.1021/es305071v
19. Duval B, Corella JP, Enrico M, Saiz-Lopez A, Cuevas CA, Adame JA et al Amouroux D (2025) Mercury isotope variability in Pyrenean lake sediments during the Late Holocene: sources, deposition, and environmental controls. ACS Earth Space Chem 9:1488–1500. https://doi.org/10.1021/acsearthspacechem.4c00402
20. Duval B, Tessier E, Kortazar L, Fernandez LA, de Diego A, Amouroux D (2023) Dynamics, distribution, and transformations of mercury species from pyrenean high-altitude lakes. Environ Res 216:114611. https://doi.org/10.1016/j.envres.2022.114611
21. Eklöf K, von Brömssen C, Huser B, Åkerblom S, Augustaitis A, Veiteberg Braaten HF et al Vuorenmaa J (2024) Trends in mercury, lead and cadmium concentrations in 27 European streams and rivers: 2000–2020. Environ Pollut 360:124761. https://doi.org/10.1016/j.envpol.2024.124761
22. Elbaz-Poulichet F, Guédron S, Anne-Lise D, Freydier R, Perrot V, Rossi M et al Sabatier P (2020) A 10,000-year record of trace metal and metalloid (Cu, Hg, Sb, Pb) deposition in a western Alpine lake (Lake Robert, France): Deciphering local and regional mining contamination. Quat Sci Rev 228:106076. https://doi.org/10.1016/j.quascirev.2019.106076
23. Enrico M, Roux GL, Marusczak N, Heimbürger L-E, Claustres A, Fu X et al Sonke JE (2016) Atmospheric mercury transfer to peat bogs dominated by gaseous elemental mercury dry deposition. Environ Sci Technol 50:2405–2412. https://doi.org/10.1021/acs.est.5b06058
24. Gascón Díez E, Corella JP, Adatte T, Thevenon F, Loizeau J-L (2017) High-resolution reconstruction of the 20th century history of trace metals, major elements, and organic matter in sediments in a contaminated area of Lake Geneva, Switzerland. Appl Geochem 78:1–11. https://doi.org/10.1016/j.apgeochem.2016.12.007
25. Gascón Roche E. (2019). *The protection of the population and the territory from technological risk: Analysis of the Monzón case*. [Bachelor's thesis]. Universidad de Zaragoza. Saragossa. Retrieved from http://zaguan.unizar.es/record/78526/files/TAZ-TFG-2019-127.pdf
26. Gaspar L, Mabit L, Lizaga I, Navas A (2020) Lateral mobilization of soil carbon induced by runoff along karstic slopes. J Environ Manag 260:110091. https://doi.org/10.1016/j.jenvman.2020.110091

27. Givelet N, Roos-Barraclough F, Shotyk W (2003) Predominant anthropogenic sources and rates of atmospheric mercury accumulation in southern Ontario recorded by peat cores from three bogs: comparison with natural “background” values (past 8000 years). J Environ Monit 5:935–949. https://doi.org/10.1039/B307140E
28. González-Sampériz P, Aranbarri J, Pérez-Sanz A, Gil-Romera G, Moreno A, Leunda M et al Valero-Garcés B (2017) Environmental and climate change in the southern Central Pyrenees since the Last Glacial Maximum: A view from the lake records. CATENA 149:668–688. https://doi.org/10.1016/j.catena.2016.07.041
29. Grousset FE, Quetel CR, Thomas B, Buat-Menard P, Donard OFX, Bucher A (1994) Transient Pb isotopic signatures in the Western European atmosphere. Environ Sci Technol 28:1605–1608. https://doi.org/10.1021/es00058a011
30. Guédron S, Audry S, Acha D, Bouchet S, Point D, Condom T et al Amouroux D (2020) Diagenetic production, accumulation and sediment-water exchanges of methylmercury in contrasted sediment facies of Lake Titicaca (Bolivia). Sci Total Environ 723:138088. https://doi.org/10.1016/j.scitotenv.2020.138088
31. Guinoiseau D, Singh SP, Galer SJG, Abouchami W, Bhattacharyya R, Kandler K et al Andreae MO (2022) Characterization of Saharan and Sahelian dust sources based on geochemical and radiogenic isotope signatures. Quat Sci Rev 293:107729. https://doi.org/doi.org/10.1016/j.quascirev.2022.107729
32. Hillman AL, Abbott MB, Valero-Garcés B, Morellon M, Barreiro-Lostres F, Bain DJ (2017) Lead pollution resulting from Roman gold extraction in northwestern Spain. The Holocene 27:1465–1474. https://doi.org/10.1177/0959683617693903
33. Hooler S, Hillman A, Hart SB, Kenney W (2025) Five decades after the Clean Air Act, legacy metal contaminants in Northeast U.S. surface waters document full recovery for the first time. Environ Pollut 373:126052. https://doi.org/10.1016/j.envpol.2025.126052
34. Horowitz HM, Jacob DJ, Amos HM, Streets DG, Sunderland EM (2014) Historical mercury releases from commercial products: global environmental implications. Environ Sci Technol 48:10242–10250. https://doi.org/10.1021/es501337j
35. Hylander LD, Meili M (2003) 500 years of mercury production: global annual inventory by region until 2000 and associated emissions. Sci Total Environ 304:13–27. https://doi.org/10.1016/S0048-9697(02)00553-3
36. Javanmardi E, Berton R (2025) Cement industry contributions to soil heavy metals accumulation: spatial patterns, seasonal trends, and geochemical controls. Int J Environ Sci Technol 22:12437–12468. https://doi.org/10.1007/s13762-025-06633-9
37. Kumar A, Abouchami W, Galer SJG, Singh SP, Fomba KW, Prospero JM, Andreae MO (2018) Seasonal radiogenic isotopic variability of the African dust outflow to the tropical Atlantic Ocean and across to the Caribbean. Earth Planet Sci Lett 487:94–105. https://doi.org/doi.org/10.1016/j.epsl.2018.01.025

38. Kylander ME, Klaminder J, Bindler R, Weiss DJ (2010) Natural lead isotope variations in the atmosphere. Earth Planet Sci Lett 290:44–53. https://doi.org/10.1016/j.epsl.2009.11.055
39. Landis MS, Keeler GJ, Al-Wali KI, Stevens RK (2004) Divalent inorganic reactive gaseous mercury emissions from a mercury cell chlor-alkali plant and its impact on near-field atmospheric dry deposition. Atmos Environ 38:613–622. https://doi.org/10.1016/j.atmosenv.2003.09.075
40. López-Vicente M, Navas A, Machín J (2009) Geomorphic mapping in endorheic catchments in the Spanish Pyrenees: an integrated GIS analysis of karstic features. Geomorphology 111:38–47. https://doi.org/10.1016/j.geomorph.2008.03.014
41. MacDonald DD, Ingersoll CG, Berger TA (2000) Development and evaluation of consensus-based sediment quality guidelines for freshwater ecosystems. Arch Environ Contam Toxicol 39:20–31. https://doi.org/10.1007/s002440010075
42. Millot R, Allègre C-J, Gaillardet J, Roy S (2004) Lead isotopic systematics of major river sediments: a new estimate of the Pb isotopic composition of the Upper Continental Crust. Chem Geol 203:75–90. https://doi.org/10.1016/j.chemgeo.2003.09.002
43. Mills K, Schillereff D, Saulnier-Talbot É, Gell P, Anderson NJ, Arnaud F et al Ryves DB (2017) Deciphering long-term records of natural variability and human impact as recorded in lake sediments: a palaeolimnological puzzle. WIREs Water 4:e1195. https://doi.org/https://doi.org/10.1002/wat2.1195
44. Monna F, Lancelot J, Croudace IW, Cundy AB, Lewis JT (1997) Pb Isotopic composition of airborne particulate material from france and the Southern United Kingdom: implications for Pb pollution sources in urban areas. Environ Sci Technol 31:2277–2286. https://doi.org/10.1021/es960870+
45. Morellón M, Morales-Molino C, Vegas J, Vicente de Vera A, Plà-Rabes S, Leunda M et al Mata MP (2025) Reconstructing the environmental impact of mining on mountain lakes. Sci Total Environ 961:178382. https://doi.org/10.1016/j.scitotenv.2025.178382
46. Morellón M, Valero-Garcés B, Anselmetti F, Ariztegui D, Schnellmann M, Moreno A et al Corella JP (2009a) Late Quaternary deposition and facies model for karstic Lake Estanya (North-eastern Spain). Sedimentology 56:1505–1534. https://doi.org/10.1111/j.1365-3091.2008.01044.x
47. Morellón M, Valero-Garcés B, González-Sampériz P, Vegas-Vilarrúbia T, Rubio E, Rieradevall M et al Soto J (2011) Climate changes and human activities recorded in the sediments of Lake Estanya (NE Spain) during the Medieval Warm Period and Little Ice Age. J Paleolimnol 46:423–452. https://doi.org/10.1007/s10933-009-9346-3
48. Morellón M, Valero-Garcés B, Moreno A, González-Sampériz P, Mata P, Romero O et al Navas A (2008) Holocene palaeohydrology and climate variability in northeastern Spain: the sedimentary record of Lake Estanya (Pre-Pyrenean range). Quat Int 181:15–31. https://doi.org/10.1016/j.quaint.2007.02.021
49. Morellón M, Valero-Garcés B, Vegas-Vilarrúbia T, González-Sampériz P, Romero Ó, Delgado-Huertas A et al Corella JP (2009b) Lateglacial and Holocene palaeohydrology in the Western Mediterranean

region: The Lake Estanya record (NE Spain). Quat Sci Rev 28:2582–2599. https://doi.org/10.1016/j.quascirev.2009.05.014

50. Navas A, López-Vicente M, Gaspar L, Machín J (2013) Assessing soil redistribution in a complex karst catchment using fallout 137Cs and GIS. Geomorphology 196:231–241. https://doi.org/10.1016/j.geomorph.2012.03.018
51. OSPAR Commission. (2019). *Mercury losses from the chlor-alkali industry in 2017*. Retrieved from https://oap.ospar.org/media/filer_public/6f/6f/6f6f87b0-568c-4826-a758-fa6329a95872/p00737_chloralkali_2017.pdf
52. Pacyna EG, Pacyna JM, Fudala J, Strzelecka-Jastrzab E, Hlawiczka S, Panasiuk D et al Friedrich R (2007) Current and future emissions of selected heavy metals to the atmosphere from anthropogenic sources in Europe. Atmos Environ 41:8557–8566. https://doi.org/10.1016/j.atmosenv.2007.07.040
53. Pey J, Larrasoaña JC, Pérez N, Cerro JC, Castillo S, Tobar ML et al Causapé J (2020) Phenomenology and geographical gradients of atmospheric deposition in Southwestern Europe: results from a multi-site monitoring network. Sci Total Environ 744:140745. https://doi.org/10.1016/j.scitotenv.2020.140745
54. Pey J, Valero-Garcés BL, Larrasoaña JC, Causapé J, de la Parra I, Reyes J et al Mata MP (2026) Geochemical fingerprinting and source apportionment of deposited African dust in southwestern Europe using elemental ratios and receptor modelling. Aeolian Res 77:101051. https://doi.org/10.1016/j.aeolia.2026.101051
55. Raldúa D, Díez S, Bayona JM, Barceló D (2007) Mercury levels and liver pathology in feral fish living in the vicinity of a mercury cell chlor-alkali factory. Chemosphere 66:1217–1225. https://doi.org/10.1016/j.chemosphere.2006.07.053
56. RD 785/2001 (2001) Real Decreto 785/2001, de 6 de julio, por el que se modifica el Real Decreto 2487/1994, de 23 de diciembre, por el que se establece la sustitución de la gasolina con plomo por gasolina sin plomo. Boletín Oficial del Estado. España. 162: 24467–24468. Retrieved from https://www.boe.es/eli/es/rd/2001/07/06/785.
57. Riera S, López-Sáez JA, Julià R (2006) Lake responses to historical land use changes in northern Spain: the contribution of non-pollen palynomorphs in a multiproxy study. Rev Palaeobot Palynol 141:127–137. https://doi.org/10.1016/j.revpalbo.2006.03.014
58. Riera S, Wansard G, Julià R (2004) 2000-year environmental history of a karstic lake in the Mediterranean Pre-Pyrenees: the Estanya lakes (Spain). CATENA 55:293–324. https://doi.org/10.1016/S0341-8162(03)00107-3
59. Rodriguez-Iruretagoiena A, Gredilla A, de Vallejuelo SF-O, Arana G, Meaurio M, Madariaga JM et al de Diego A (2023) Metals and metalloids in high-altitude Pyrenean lakes: sources and distribution in pre-industrial and modern sediments. Environ Sci Pollut Res 30:87561–87574. https://doi.org/10.1007/s11356-023-28347-6

60. Rodriguez-Veiga I, Pey J, Garralón A, Valero-Garcés BL, Schmid T, Saiz-Lopez A et al Corella JP (2026) Mercury and lead legacy pollution from a coal-fired power plant recorded in lake Chiprana sedimentary record (NE Spain). J Soils Sediments 26:250. https://doi.org/10.1007/s11368-026-04448-w
61. Rosca C, Junginger A, Kübler S, Babechuk MG, Olaka LA, Schoenberg R (2024) Isotopic and trace element record of changing metal source contributions to tropical freshwater Lake Naivasha (Kenya). Sci Total Environ 951:175082. https://doi.org/10.1016/j.scitotenv.2024.175082
62. Rosman KJR, Chisholm W, Hong S, Candelone J-P, Boutron CF (1997) Lead from Carthaginian and Roman Spanish mines isotopically identified in Greenland ice dated from 600 B.C. to 300 A.D. Environ Sci Technol 31:3413–3416. https://doi.org/10.1021/es970038k
63. Sabatier P, Moernaut J, Bertrand S, Van Daele M, Kremer K, Chaumillon E, Arnaud F (2022) A review of event deposits in lake sediments. Quaternary 5:34. https://doi.org/10.3390/quat5030034
64. Sakata M, Marumoto K, Narukawa M, Asakura K (2006) Regional variations in wet and dry deposition fluxes of trace elements in Japan. Atmos Environ 40:521–531. https://doi.org/10.1016/j.atmosenv.2005.09.066
65. Sakata M, Tani Y, Takagi T (2008) Wet and dry deposition fluxes of trace elements in Tokyo Bay. Atmos Environ 42:5913–5922. https://doi.org/10.1016/j.atmosenv.2008.03.027
66. Sancho Marcén C (1988) El polje de Saganta (Sierras Exteriores pirenaicas, prov. de Huesca). Cuatern Geomorfol 2:107–113.
67. Schwikowski M, Barbante C, Doering T, Gaeggeler HW, Boutron C, Schotterer U et al Cescon P (2004) Post-17th-century changes of European lead emissions recorded in high-altitude alpine snow and ice. Environ Sci Technol 38:957–964. https://doi.org/10.1021/es034715o
68. Semertzidou P, Piliposian GT, Appleby PG (2016) Atmospheric residence time of 210Pb determined from the activity ratios with its daughter radionuclides 210Bi and 210Po. J Environ Radioact 160:42–53. https://doi.org/10.1016/j.jenvrad.2016.04.019
69. Souza EJdS, Fomba KW, Anaya SGM, Schepanski K, Freire SM, Materić D et al Herrmann H (2025) Particle-bound mercury in Saharan dust-loaded particulate matter in Cabo Verde. J Hazard Mater 487:137053. https://doi.org/10.1016/j.jhazmat.2024.137053
70. Streets DG, Horowitz HM, Jacob DJ, Lu Z, Levin L, ter Schure AFH, Sunderland EM (2017) Total mercury released to the environment by human activities. Environ Sci Technol 51:5969–5977. https://doi.org/10.1021/acs.est.7b00451
71. U.S. EPA (1996) Method 3050B: acid digestion of sediments, sludges, and soils. Revision 2. Washington, DC.
72. U.S. EPA (1998) Method 7473 (SW-846): mercury in solids and solutions by thermal decomposition, amalgamation, and atomic absorption spectrophotometry. Revision 0. Washington, DC.
73. U.S. EPA (2014) EPA Positive Matrix Factorization (PMF) 5.0 fundamentals and user guide. EPA/600/R-14/108. Washington, DC.

74. Valero-Garcés B, Morellón M, Puertas C, Moreno A, Corella J, Gonzalez Samperiz P et al Navas A (2009) Una visión paleolimnológica de tres lagos kársticos (Zoñar, Estanya y Taravilla): evolución sedimentaria y paleohidrológica, clima e impacto humano e implicaciones para la gestión y conservación. Bol Geolog Min 120.

Figures

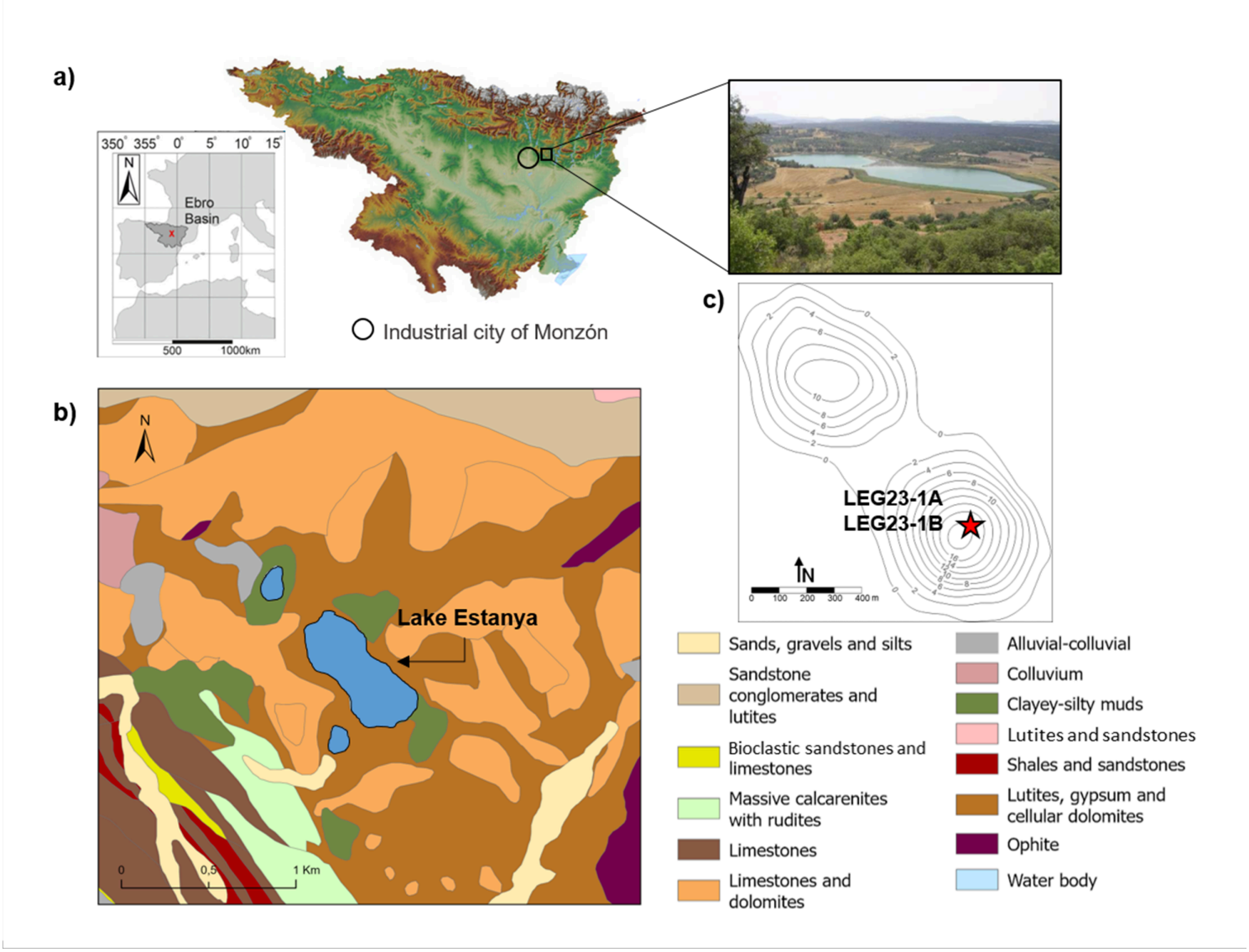


Figure 1

Composite figure illustrating: a) Detail of the Ebro basin showing both locations of Lake Estanya (▯) and Monzón industrial complex (○). On the right, the Lake Estanya panoramic view (Pérez-Sanz, 2014; CHE). b) Lithological map of the area surrounding the three dolines of the Estanya karstic lake complex. The main doline, referred to in this study as Lake Estanya, is indicated on the map. c) Bathymetric map of Lake Estanya (modified from Morellón et al. 2011). LEG23-1A and LEG23-1B coring sites are shown

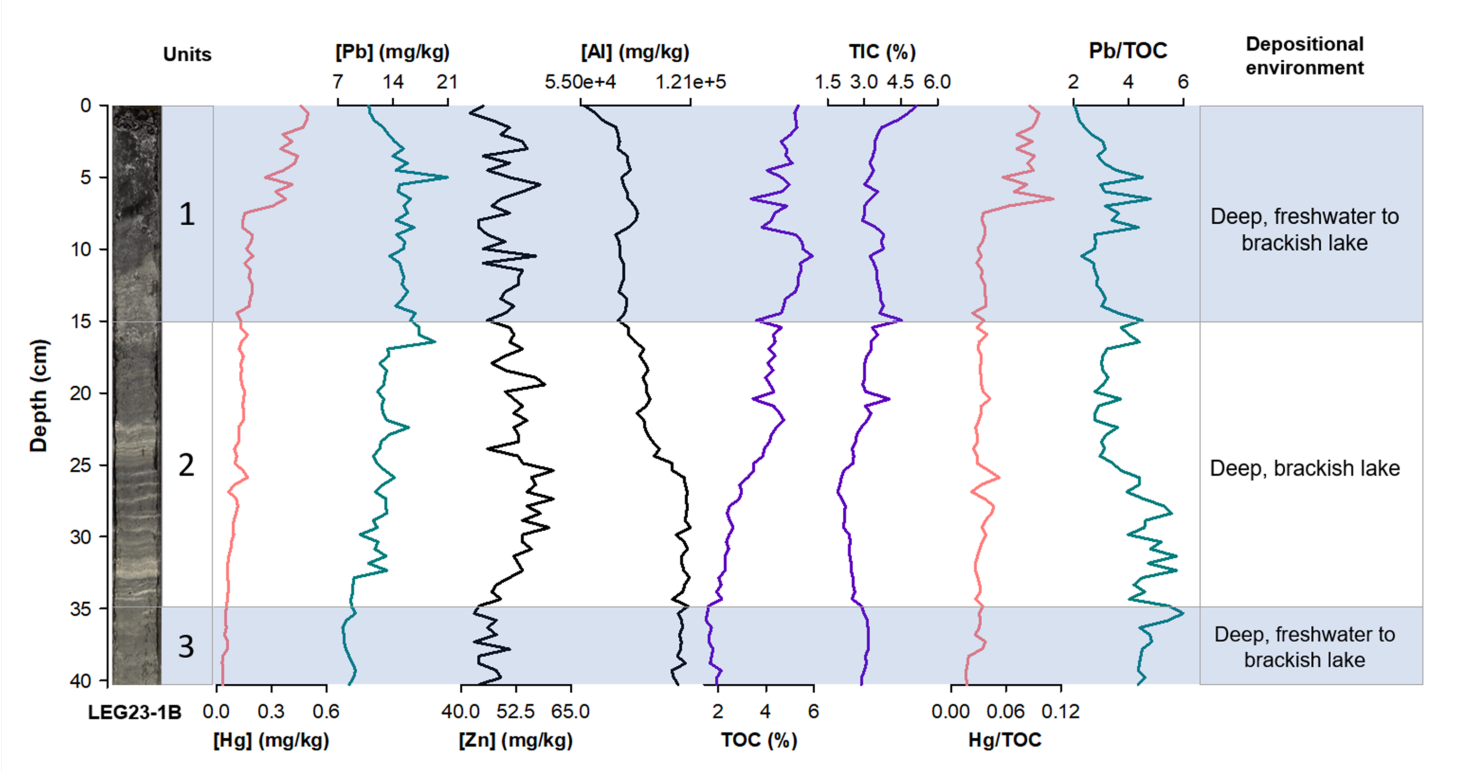


Figure 2

Vertical profiles of Hg, Pb, Al, and Zn concentrations, along with TIC and TOC weight percentages and normalised ratios (Hg/TOC and Pb/TOC). The right panel provides a summary of the depositional environments associated with each stratigraphic unit

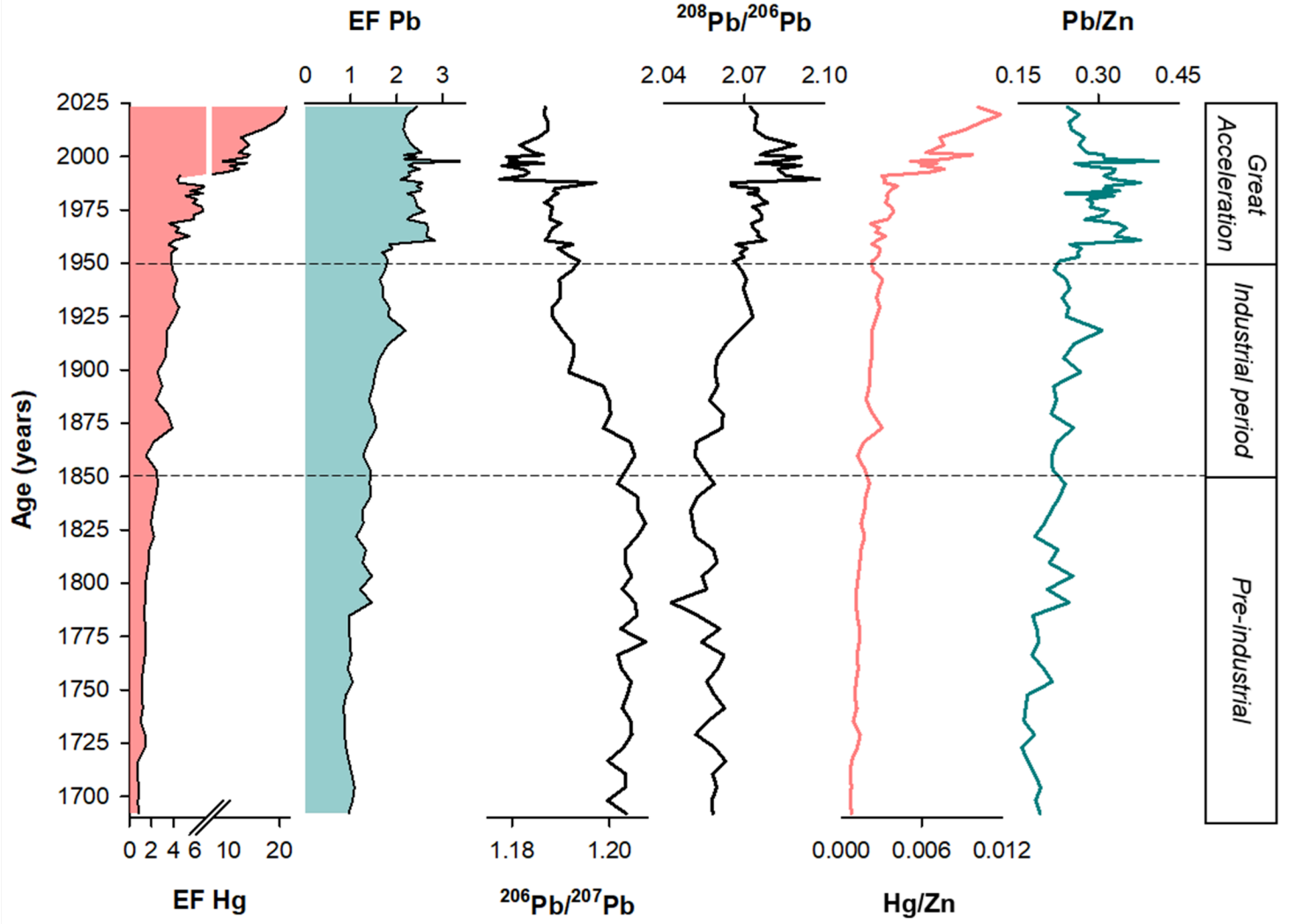


Figure 3

Evolution of Hg and Pb enrichment factors in Lake Estanya. Age-related variations in lead isotopic ratios ($^{206}Pb/^{207}Pb$, $^{208}Pb/^{206}Pb$) as well as elemental ratios (Hg/Zn, Pb/Zn) are also displayed

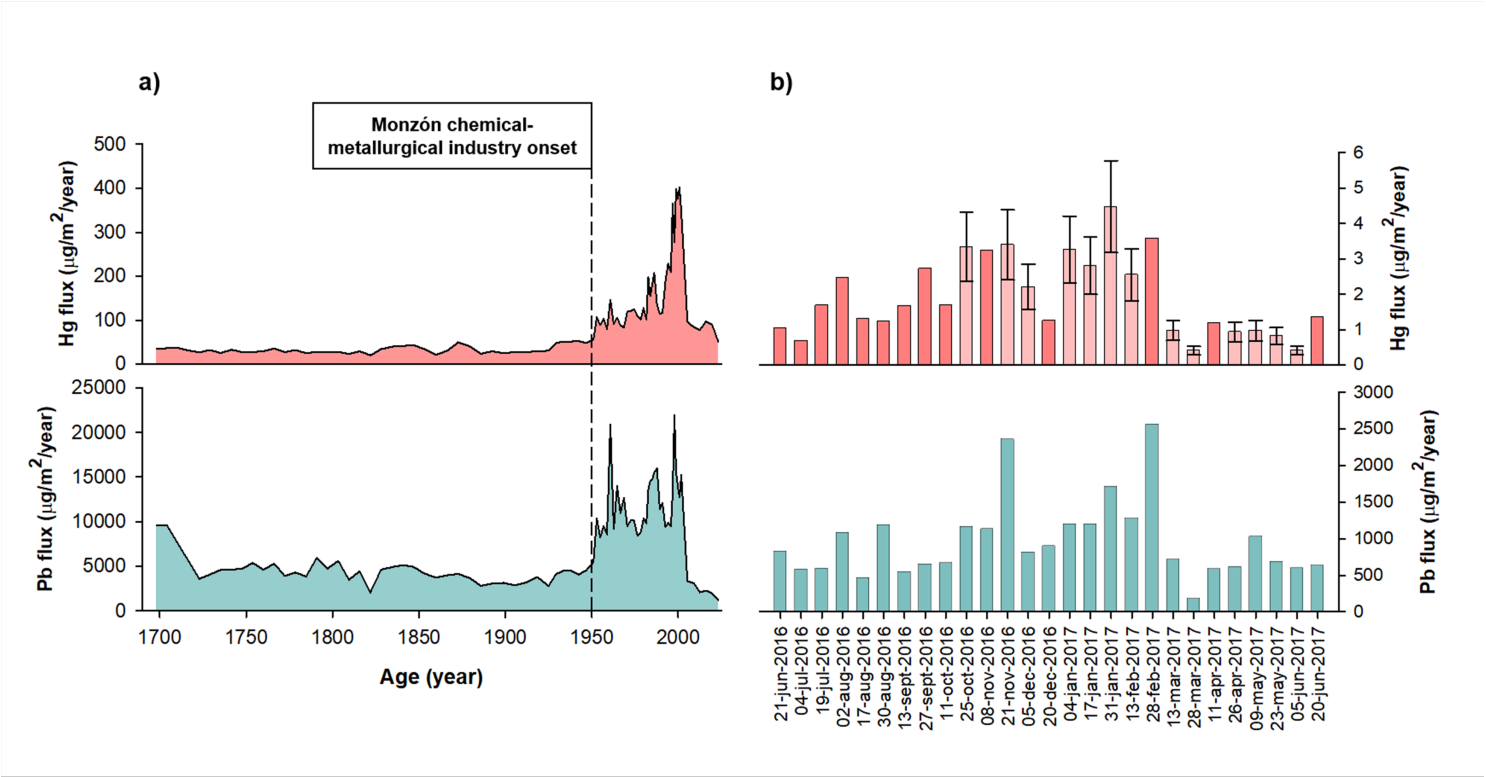


Figure 4

a) Evolution of Hg and Pb fluxes in sediments of Lake Estanya over the last ~330 years. b) Atmospheric Hg and Pb deposition fluxes (expressed in μg m^{-2} $year^{-1}$) registered during the studied period (June 2016–June 2017) at the Monzón site of the DONAIRE network. Hg flux ranges estimated via correlation with Fe, Mn, and Sr are displayed as lighter-coloured bars with associated error bars

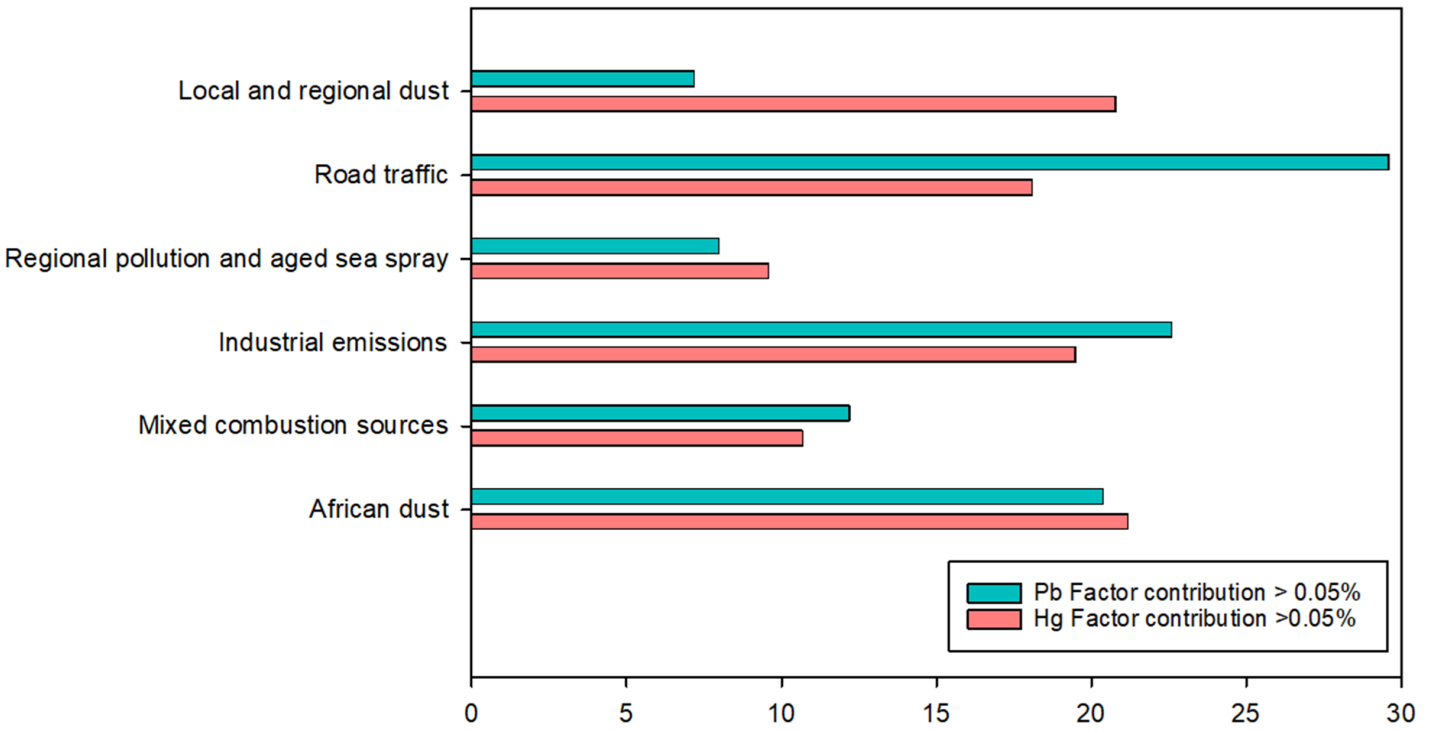


Figure 5

Primary sources of atmospheric deposition pollutants identified in the Monzón site of the DONAIRE network between June 2016 and June 2017

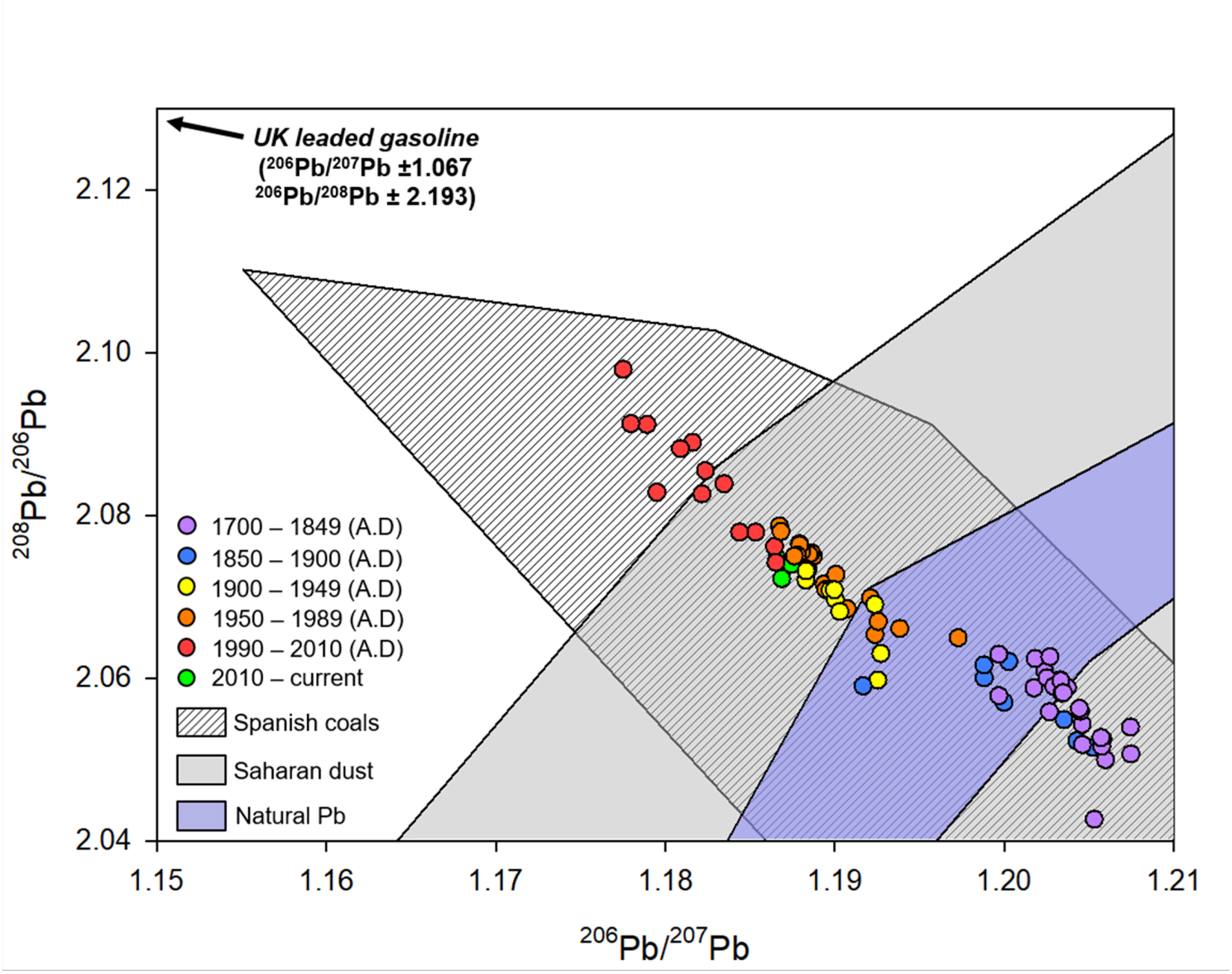


Figure 6

Three-isotope plot of $^{206}Pb/^{207}Pb$ vs. $^{208}Pb/^{206}Pb$ ratios showing the isotopic compositions of Lake Estanya sediments. The historical periods are indicated by colour. For reference, Pb isotopic composition ranges of UK leaded gasoline (not showed, (Monna et al. 1997)); Spanish coals (striped pattern (Díaz-Somoano et al. 2007)); Saharan dust (shaded area, (Grousset et al. 1994; Kumar et al. 2018; Guinoiseau et al. 2022)) and natural Pb (coloured area, (Rosman et al. 1997; Millot et al. 2004; Kylander et al. 2010; Adánez Sanjuán et al. 2018)) are also presented

Supplementary Files

This is a list of supplementary files associated with this preprint. Click to download.

- CopiadeESM2.SourceapportionmentMonzn.xlsx
- ESM1.docx